Journal of Materials Chemistry A

ROYAL SOCIETY OF CHEMISTRY

PAPER

View Article Online
View Journal | View Issue

Cite this: *J. Mater. Chem. A*, 2024, **12**, 3557

Boosting electrocatalytic hydrogen evolution over a Mo_2C–W_2C heterostructure by interface-induced electron modulation†

Lijuan Jiang, Ruijing Wang, Huimin Zhou, Guang-Feng Wei* and Xuefeng Wang *

Carbides have a high d-band electronic density of states at the Fermi level and hence characteristics resembling those of platinum. However, due to the strong adsorption of hydrogen intermediates on the surface of the carbides, the kinetics of the hydrogen evolution reaction (HER) is severely limited. Here, we demonstrate a strategy to improve the HER kinetics of carbides by modulating the surface electronic structure. Mo_2C–W_2C ultrafine nanoparticles on reduced graphene oxide (Mo_2C–W_2C/RGO) with strong electron interaction are constructed to improve the HER activity. The interfacial interaction between Mo_2C and W_2C adjusts the electronic structure of the surface, and the favorable hydrogen desorption on this surface is proved by density functional theory calculations. Benefitting from the adjusted electronic structures on the Mo_2C–W_2C heterointerface, the hydrogen adsorption free energies on both the Mo and W sites of Mo_2C–W_2C are close to the ideal values (0 eV). As expected, the Mo_2C–W_2C/RGO exhibits a superior HER activity with ultra-low overpotentials of 81 mV and 87 mV at a current density of -10 mA cm^{-2} under acidic and alkaline conditions, respectively, as well as remarkable stability. This work reveals the modulating effect of the electronic structure of carbides on the HER activity, which has a profound guiding effect for the directional design of advanced electrocatalysts.

Received 29th November 2023
Accepted 30th December 2023

DOI: 10.1039/d3ta07373d

rsc.li/materials-a

Introduction

The hydrogen evolution reaction (HER) *via* water electrolysis enables the conversion of renewable energy sources (such as tidal, solar, wind, and geothermal energy) into green H_2 energy, offering a promising route to alleviate the excessive consumption of fossil fuels and related environmental issues.[1,2] In order to reduce the reaction energy barrier and overpotential, electrocatalysts play a crucial role in the process of water electrolysis.[3–5] The HER is a classic two-electron reduction process with hydrogen intermediates (H*) as the only reaction intermediate ($2H^+ + 2e^- \rightarrow H_2$ in acidic solution or $2H_2O + 2e^- \rightarrow H_2 + 2OH^-$ in alkaline solution).[6] According to the Sabatier principle,[7] an active HER catalyst generally binds hydrogen neither too weakly nor too strongly, regardless of the pH value of the reaction solution. Currently, Pt group noble metals are considered as benchmark HER electrocatalysts showing extremely low overpotential.[8–10] Unfortunately, their low abundance and high price hinder their large-scale application; thus, exploiting earth-abundant and high-performance HER electrocatalysts is inevitable.

Remarkable advances have been made regarding the use of transition metals and their alloys, carbides, nitrides, chalcogenides, and phosphides, which feature their high activity, outstanding stability, and earth abundance.[11,12] Among the candidates, transition-metal carbides, such as molybdenum carbides and tungsten carbides, have attracted increasing interest on account of their noble-metal-like electronic configuration, high electronic conductivity, wide pH applicability and outstanding catalytic activity correlated with tunable phase composition.[13,14] In addition, a previous report has proposed that the hybridizing between the d-orbital of metallic tungsten/molybdenum atoms and s- or p-orbital of carbon atoms gave rise to a broadened d-band of molybdenum carbides and tungsten carbides resulting in high similarity to the d-band of Pt.[15–18] Despite its unique properties, pure carbides show low activity for the HER.[19] On the one hand, density functional theory (DFT) calculations have demonstrated that the strong adsorption of H* on the carbide surface facilitates the reduction of H^+ but restricts the hydrogen desorption step.[20] On the other hand, the synthesis of carbides usually requires a high-temperature annealing process, resulting in serious agglomeration of particles to form an irregular morphology with low specific surface area, thereby reducing the density of the active site.[21,22] Efforts have been devoted to designing carbide nanostructures with large surface area and well-exposed active sites. For instance, Hu *et al.* reported a scalable and economical method to produce W_2C nanodot-decorated CNT networks *via*

Shanghai Key Lab of Chemical Assessment and Sustainability, School of Chemical Science and Engineering, Tongji University, Shanghai 200092, China. E-mail: weigf@tongji.edu.cn; xfwang@tongji.edu.cn

† Electronic supplementary information (ESI) available. See DOI: https://doi.org/10.1039/d3ta07373d

a spray-drying approach.[23] Zheng *et al.* presented a strategy to synthesize well-dispersed transition metal carbide nanoparticles.[24] These strategies have been successfully used to prepare a variety of carbide nanomaterials with effectively improved activity, but the size of the as-obtained nanoparticles is hard to control and the size distribution range is wide. At the same time, these strategies for adjusting the nanoarchitectures of carbides cannot change their inherent properties of the strong adsorption of hydrogen intermediates, which also leads to the limitation of the activity of carbides. To address this issue, numerous approaches are being pursued to modify carbides by constructing heterophases and doping with heteroatoms to adjust the electronic properties and enhance the HER activity.[19,20,25,26] Notably, the strong interaction at the two-phase interface can establish electronic transfer and generate electronic density redistribution between the two adjacently contacted components, adjusting the electronic structure and promoting electrocatalytic performance. Chen *et al.* identified that a synergy between Mo_2N and Mo_2C in biomass-derived heterostructures can exert the activity and satisfactory durability.[25] From this perspective, constructing small-sized carbide nanoarchitectures and modulating the electronic structure of carbides should be an effective way to branch out for studying catalytic abilities.

Herein, a heterostructure composed of Mo_2C and W_2C anchored to reduced graphene oxide (denoted as Mo_2C–W_2C/RGO) is constructed *via* a sequential two-step approach. The Mo_2C–W_2C heterostructure with ultrafine size (about 2–3 nm) and abundant interfaces maximizes the exposure of active sites and facilitates the mass transfer process, while the interfacial interaction optimizes the electronic configuration of the catalyst. DFT calculations reveal the modulating effect of the electronic structure of the Mo_2C–W_2C heterostructure on the HER activity. The Mo_2C–W_2C heterostructure shows a favourable hydrogen desorption step, resulting in the optimized free energy for hydrogen adsorption (ΔG_{H^*}). As expected, the Mo_2C–W_2C/RGO affords an ultra-low overpotential (η_{10} = 81 and 87 mV for reaching a current density of −10 mA cm^{-2}) under acidic and alkaline conditions.

Materials and methods

Chemicals

The graphene oxide (GO) powder was obtained from Qitaihe Baotailong Graphene New Material Co., Ltd. Ammonium metatungstate hydrate ($(NH_4)_6H_2W_{12}O_{40}\cdot xH_2O$), ammonium molybdate tetrahydrate ($(NH_4)_6Mo_7O_{24}\cdot 4H_2O$), melamine and potassium hydroxide (KOH) were purchased from Aladdin. Concentrated sulfuric acid (H_2SO_4) and ethanol were purchased from Sinopharm Chemical Reagent Co., Ltd. Nafion solution (5%) was purchased from Sigma-Aldrich.

Synthesis of electrocatalysts

Take Mo_2C–W_2C/RGO-0.56 as an example: GO (0.20 g), $(NH_4)_6Mo_7O_{24}\cdot 4H_2O$ (0.36 g), $(NH_4)_6H_2W_{12}O_{40}\cdot xH_2O$ (0.50 g) and melamine (2.0 g) in double-distilled water (40 mL) were sonicated for 60 min. Then, after drying at 80 °C for a whole night, the obtained well-mixed precursor powder was pyrolyzed at 800 °C under Ar flow for 3 h, and the Mo_2C–W_2C/RGO catalyst was produced. According to the varied Mo/W molar ratio, a series of Mo_2C–W_2C/RGO were obtained, the products were denoted as Mo_2C–W_2C/RGO-*n*, in which *n* refers to the measured $n_{Mo/(Mo+W)}$. According to a similar procedure, Mo_2C/RGO and W_2C/RGO were obtained in the absence of $(NH_4)_6H_2W_{12}O_{40}\cdot xH_2O$ and $(NH_4)_6Mo_7O_{24}\cdot 4H_2O$, respectively. Graphene oxide (GO) was directly annealed in an Ar atmosphere at 800 °C for 3 h to obtain reduced graphene oxide (RGO).

Material characterization

Scanning electron microscopy (SEM) was performed on a Hitachi S-4800 instrument. Transmission electron microscopy (TEM), high-resolution transmission electron microscopy (HRTEM), energy dispersive X-ray spectroscopy (EDS), and elemental mapping investigations were performed with a JEOL JEM 2100 instrument. X-ray diffraction (XRD) analysis was performed on a Bruker D8 diffractometer using Cu Kα radiation (λ = 1.54056 Å). X-ray photoelectron spectroscopy (XPS) was conducted on a Thermo Scientific™ K-Alpha™⁺ spectrometer equipped with a monochromatic Al Kα X-ray source (1486.6 eV) operating at 100 W. All peaks were calibrated to the C 1s peak binding energy at 284.8 eV for adventitious carbon. The Raman investigation was performed on a laser confocal Raman microspectrometer (XploRA, Horiba Jobin Yvon, Ltd.)

Electrochemical measurements

All electrochemical measurements were performed using an electrochemical workstation (CHI 660, CH Instruments, Inc., Shanghai, China) in a three-electrode system. As for the HER test, the graphite rod and saturated calomel electrode (SCE, Hg/Hg_2Cl_2 in saturated KCl) were used as the counter electrode and reference electrode, respectively. The synthesized samples (5 mg) were first dispersed in 1.0 mL of ethanol mixture and 30 μL of 5 wt% Nafion solution prior to $a \geq 30$ min sonication to form an electrocatalyst ink and then loaded onto a glassy carbon electrode (GCE, 4 mm in diameter) as a working electrode. The potential values used in this study were converted to $E_{(RHE)}$ from $E_{(SCE)}$ according to the formula $E_{(RHE)} = E_{(SCE)} + 0.241 + 0.059 \times$ pH. For comparison, commercial 20 wt% Pt/C with the same mass loading was also tested. Linear sweep voltammetry (LSV) tests for the HER were conducted with a scan rate of 5 mV s^{-1} in electrolytes (0.5 M H_2SO_4 or 1.0 M KOH). The double-layer capacitances (C_{dl}) were calculated through cyclic voltammograms (CV) at various sweep rates from 20 to 200 mV s^{-1}. Electrochemical impedance spectroscopy (EIS) was carried out at an overpotential of 200 mV in a frequency range from 10^{-2} Hz to 10^5 Hz and an amplitude of 5 mV.

Computation details

The generalized gradient approximation (GGA) with the Perdew–Burke–Ernzerhof (PBE) exchange–correlation functional[27] and a 450 eV cutoff for the plane-wave basis set[28] were employed to perform all the density functional theory (DFT) computations

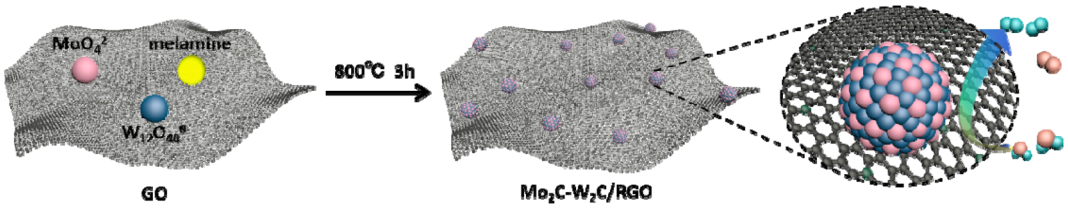

Fig. 1 Schematic illustration for fabricating Mo_2C–W_2C/RGO.

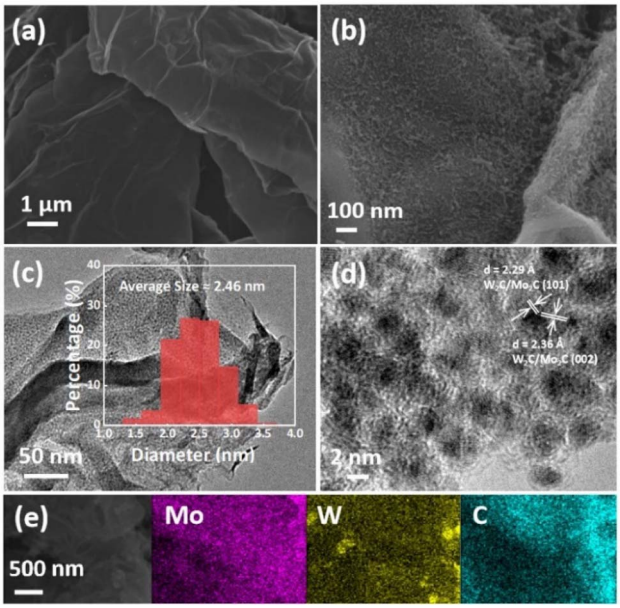

Fig. 2 SEM images of (a) RGO and (b) Mo_2C–W_2C/RGO-0.56. (c) TEM image and (d) HR-TEM image of Mo_2C–W_2C/RGO-0.56. (e) SEM image and corresponding element mappings of Mo_2C–W_2C/RGO-0.56. The inset in panel (c) is the size distribution diagram.

of the materials within the framework of VASP packages[29] with projector augmented wave (PAW) pseudopotentials.[30] The Monkhorst–Pack *k*-point mesh with a maximum spacing of 0.05 Å was utilized for the first Brillouin zone integrations.[31] The DFT-D3(BJ) method of Grimme was employed to describe long-range van der Waals interactions.[32,33] To correct the zero-point energy for the reaction barrier, the vibrational frequency calculations were performed *via* the finite-difference approach. (2 × 2) four-layer slab models were utilized to simulate the exposed (001) surfaces of Mo_2C and W_2C. The top two layers of the slab models were fully relaxed and the other layers were fixed to the bulk structure. Due to the small lattice mismatch (<1%), the junction between W_2C (001) and Mo_2C (001) with two layers at each side was used to build the theoretical model of the Mo_2C–W_2C interface. The convergence criterion for an electronic self-consistent iteration was set at 1.0×10^{-5} eV. The Quasi-Newton lBFGS method was used for geometry relaxation until the maximal force became less than 0.01 eV $Å^{-1}$.

The Gibbs free energy changes (ΔG) for hydrogen adsorption were expressed as:

$$\Delta G = \Delta E + \Delta \mathrm{ZPE} - T\Delta S + \int_0^{298.15\mathrm{K}} \Delta C_V \mathrm{d}T$$

where ΔE is the adsorption energy of H on the surface, ΔZPE is the zero-point vibrational energy difference between the adsorbed state and the gas phase state, ΔC_V is the heat capacity difference, T is the temperature (298.15 K), and ΔS is the entropy difference. The standard thermodynamic data[34] were utilized to obtain the temperature and pressure contributions.

Results and discussion

The synthesis of Mo_2C–W_2C/RGO is schematically depicted in Fig. 1. According to the varied Mo/W molar ratio, the products were denoted as Mo_2C–W_2C/RGO-*n*, in which *n* refers to the measured $n_{Mo/(Mo+W)}$ (Table S1†). Mo_2C/RGO and W_2C/RGO were prepared by similar synthesis methods for comparison. The morphologies of the samples were investigated by scanning electron microscopy (SEM) and transmission electron microscopy (TEM). The SEM image of RGO in Fig. 2a shows the morphology of nanosheets with ripples. We further examined the nanoscale structure of Mo_2C–W_2C/RGO. Taking Mo_2C–W_2C/RGO-0.56 as a model sample, numerous well-distributed and ultrafine Mo_2C–W_2C nanoparticles (about 2.46 nm in average size, inset of Fig. 2c) are anchored to the graphene sheets (Fig. 2b and c). The smaller particle size and uniform nature of Mo_2C–W_2C would effectively reduce the loss of active sites and promote fast mass transfer. Similarly, Mo_2C/RGO, Mo_2C–W_2C/RGO-0.75, Mo_2C–W_2C/RGO-0.24, and W_2C/RGO also displayed ultrafine nanoparticles (Fig. S1†). The lattice fringes with spacings of 2.36 Å and 2.29 Å nm observed in Fig. 2d are associated with the (002) crystal facet and the (101) crystal facet of Mo_2C or W_2C; the high-resolution TEM (HR-TEM) image also demonstrates that abundant interfaces exist in the structure owing to the alternative arrangement of Mo_2C and W_2C nanocrystals. In addition, the energy-dispersive X-ray spectra (EDS) manifest that the Mo_2C–W_2C/RGO composites were composed of Mo, W, C, N and O elements (Fig. S2†), with a small amount of N doped from melamine. The O element results from the inevitable oxidation caused by exposure to air. Furthermore, the elemental mapping of W, Mo, and C from the SEM image (Fig. 2e) indicates a uniform spatial distribution throughout the whole scanning region, confirming the homogeneous growth of Mo_2C–W_2C.

The XRD investigation confirmed the formation of Mo_2C–W_2C/RGO heterostructures in the final products (Fig. 3a), and the results of Mo_2C/RGO, W_2C/RGO and Mo_2C–W_2C/RGO show

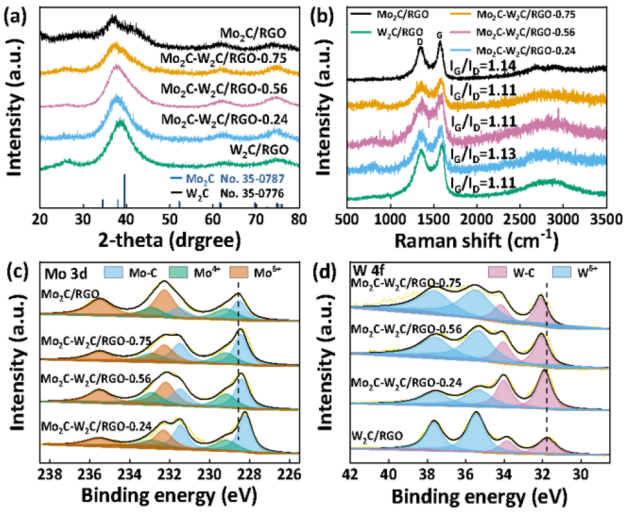

Fig. 3 (a) XRD patterns and (b) Raman spectra of the Mo_2C/RGO, W_2C/RGO and all Mo_2C–W_2C/RGO samples. XPS profiles of (c) Mo 3d and (d) W 4f in the Mo_2C/RGO, W_2C/RGO and all Mo_2C–W_2C/RGO samples.

the characteristic pattern of hexagonal W_2C (JCPDS no. 35-0776) and Mo_2C (JCPDS no. 35-0787). The diffraction peaks of all samples are relatively weak and broad, consistent with the ultrafine nanoparticles shown by SEM and TEM results. Accordingly, these samples present two distinct characteristic peaks of the carbon-based networks, located in the D (1350 cm^{-1}) and G (1580 cm^{-1}) bands in Raman spectra (Fig. 3b).[35,36] The I_G/I_D value for GO sheets (1.25) is significantly higher than that for RGO nanosheets (0.98) because of the decrease in oxygenic groups during the thermal treatment (Fig. S3†). In contrast, the I_G/I_D values of Mo_2C–W_2C/RGO, W_2C/RGO, and Mo_2C/RGO are markedly increased compared with RGO, which could be due to the coupling between carbide nanoparticles and RGO resulting in a more disordered carbon structure.

To analyze the surface chemical composition and electronic structure of the samples, X-ray photoelectron spectroscopy (XPS) was performed. As depicted in Fig. S4a,† an XPS survey was used to identify the composition of the Mo, W, and C elements in these samples. The profiles of Mo 3d in Mo_2C–W_2C/RGO and Mo_2C/RGO can be deconvoluted into six peaks (Fig. 3c), suggesting that there are three species (Mo–C, Mo^{4+}, and Mo^{6+}) for Mo on the surface.[37,38] For the Mo_2C/RGO sample, the couple at 228.5 and 231.5 eV should be ascribed to the Mo $3d_{5/2}$ and $3d_{3/2}$ of Mo–C species. The peaks located at 229.2 and 232.9 eV are attributed to Mo^{4+} species, and the two at 232.2 and 235.5 eV are associated with Mo^{6+} species. They are commonly observed when carbides are exposed to air.[39] The W 4f spectrum of W_2C/RGO (Fig. 3d) can be fitted into four peaks with binding energies at 35.5 and 37.7 eV corresponding to W $4f_{7/2}$ and $4f_{5/2}$ of surface oxidized W^{6+}, while the two peaks at 31.8 and 33.8 eV can be attributed to W $4f_{7/2}$ and $4f_{5/2}$ of W–C species.[40] Similarly, Mo 3d and W 4f for all Mo_2C–W_2C/RGO samples can also be fitted into corresponding peaks. Regarding the consistent binding energy of the oxidation state affected by air (Mo^{6+}, Mo^{4+} and W^{6+}) in the peak fitting of all the samples, we focus on the binding energy of Mo–C and W–C species affected by the heterostructure, which are regarded as the active centers for electrocatalytic HER.[40,41] The Mo_2C/RGO sample presents Mo $3d_{5/2}$ and $3d_{3/2}$ at 228.5 and 231.5 eV for Mo–C species, respectively. By contrast, these peaks for Mo–C species slightly shift toward lower binding energies in all Mo_2C–W_2C/RGO samples, indicating that a change in the electronic structure occurs due to introduction of the W_2C. On the other hand, the binding energy of the W–C species of Mo_2C–W_2C/RGO is positively shifted from that of W_2C/RGO samples. Given the higher electronegativity of Mo (2.16) compared to W (1.7),[42] the negative shift of Mo–C and positive shift of W–C species in all Mo_2C–W_2C/RGO samples can reasonably be attributed to electron transfer from W to Mo. Notably, the binding energies of Mo shifted negatively with increasing W composition in Mo_2C–W_2C/RGO, suggesting that the electronic structure of the surface of the samples can be effectively modified by varying the Mo/W ratio (Fig. 3c and d). The above high-resolution XPS analysis shows that the construction of the Mo_2C–W_2C/RGO heterostructure modulates the electronic structure of the original carbide, which is expected to regulate the adsorption/desorption strength between active sites and adsorbates. Fig. S4b† shows the high-resolution C 1s XPS spectrum for the all samples, which can be deconvoluted into five peaks (C–C/C=C, C–N, C=O, O=C–O, and C–Mo/C–W).[43,44] Moreover, the N 1s XPS profile (Fig. S4c†) can be fitted into four peaks, assigned to Mo 3p, pyridinic-N, pyrrolic-N, and quaternary-N, respectively.[45–47] In general, the planar structures of pyrrolic-N and pyridinic-N favor electron transport in π–π-conjugated graphite layers.[40] Regarding the similarity in N type and content, the contribution to conductivity by N-doping into the carbon matrix can be considered to be equivalent for W_2C/RGO, Mo_2C/RGO, and all Mo_2C–W_2C/RGO samples.

The electrocatalytic HER performances of the samples were first evaluated in the standard three electrode system under 0.5 M H_2SO_4 conditions at 5 mV s^{-1}. All the samples are supported on glassy carbon electrodes with the same mass loading of 0.24 mg cm^{-2}. The synthesis conditions of different molar ratios of W and Mo are at first screened (Fig. S5†), and all the Mo_2C–W_2C/RGO materials are superior to the W_2C/RGO and Mo_2C/RGO (Fig. S5 and Table S2†). At the same time, it is suggested that the optimal electrocatalyst with an appropriate Mo/W molar ratio is Mo_2C–W_2C/RGO-0.56. Fig. 3a displays the polarization curves of the W_2C/RGO, Mo_2C–W_2C/RGO-0.56 and Mo_2C/RGO, along with bare RGO and the commercial Pt/C (20 wt%) benchmark for reference. It is obvious that RGO has a negligible HER activity. The W_2C/RGO and Mo_2C/RGO afford overpotentials (η_{10}) of 158 mV and 110 mV to achieve a current density (j) of −10 mA cm^{-2}, and Mo_2C–W_2C/RGO-0.56 exhibits an ultralow η_{10} of only 81 mV. This result reveals that the unique two-phase heterostructure under an optimal Mo/W ratio can dramatically boost the catalytic activity. In addition, the catalytic performance of Mo_2C–W_2C/RGO-0.56 is much better than those of molybdenum- and/or tungsten-based multi-phase heterostructures at −10 mA cm^{-2}, such as twinned WCN (128

mV),[48] W_2C/WP@NC (116.37 mV),[49] Mo_2N–Mo_2C/HGr (157 mV),[50] and WC-W_2C/HCDs (96 mV),[51] and is the best among the non-noble catalysts reported recently (Table S3†).

To further investigate the HER mechanism, the Tafel plots (Fig. 4b) were derived by plotting the overpotential against log(j) according to the Tafel equation ($\eta = b \times \log(j) + a$).[52] Mo_2C–W_2C/RGO-0.56 delivers a low onset overpotential (η_{onset}) of 30 mV and a low Tafel slope (b) of 56 mV dec^{-1}, superior to those of Mo_2C/RGO (η_{onset} = 43 mV, b = 73 mV dec^{-1}) and W_2C/RGO (η_{onset} = 67 mV, b = 94 mV dec^{-1}). Generally, the HER process includes two steps, namely the Volmer, Heyrovsky or Tafel steps,[1,53] corresponding to Tafel slopes of 120, 40, and 30 mV dec^{-1}, respectively. The above results suggest that the HER kinetics for Mo_2C–W_2C/RGO-0.56, Mo_2C/RGO and W_2C/RGO should follow the Volmer–Heyrovsky mechanism and Mo_2C–W_2C/RGO-0.56 suggests a more rapid HER kinetics.[54,55] Extrapolating the above Tafel plots, the higher value of the calculated exchange current density (j_0) also indicates the high HER activity of Mo_2C–W_2C/RGO-0.56 (Table S4†).

The electrochemically active surface area (ECSA) of the samples was estimated by the double layer capacitance (C_{dl}).[56,57] In accordance with the obtained C_{dl} values (Fig. S6†), Mo_2C–W_2C/RGO-0.56 (38.5 mF cm^{-2}) has the highest ECSA of all samples, thereby further confirming the higher performance of Mo_2C–W_2C/RGO-0.56. In addition, the electrochemical impedance spectroscopy (EIS) measurements (Fig. 4c) show that Mo_2C–W_2C/RGO-0.56 has the smallest electron transfer resistance and the EIS trend is in good agreement with the HER activity trend. The HER activity of the above samples along with that of the commercial Pt/C catalyst is summarized in Table S4.†

As another important assessment of the electrocatalyst, a long-term electrochemical stability test of Mo_2C–W_2C/RGO-0.56 in acidic media was also performed (Fig. 4d). The activity of the working electrode remained almost completely stable in the continuous test of 30 h, and the polarization curve of the catalyst after the stability test showed no measurable decline of the cathodic current (inset of Fig. 4d). Accordingly, SEM investigation confirmed the well-retained nanostructures after the stability test, as shown in Fig. S7.† These results demonstrate that Mo_2C–W_2C/RGO-0.56 possesses outstanding durability in acidic electrolyte.

Additionally, Mo_2C–W_2C/RGO-0.56 also exhibited good HER performance in the alkaline medium (Fig. 5 and Table S5†). Apparently, the performance improvement after the formation of the Mo_2C–W_2C heterostructure can be obviously observed from Fig. S8 and Table S6.† By contrast, Mo_2C–W_2C/RGO-0.56 displays a relatively small overpotential of 87 mV at −10 mA cm^{-2}, lower than those of Mo_2C/RGO (134 mV), W_2C/RGO (159 mV), and RGO (491 mV). Besides, commercial Pt/C still presents the best HER performance, requiring an overpotential of merely 27 mV to deliver a current density of −10 mA cm^{-2}. The faster HER kinetics of Mo_2C–W_2C/RGO-0.56 can be reflected by its small Tafel slope of 59 mV dec^{-1} and low onset overpotential of 33 mV, lower than the values of Mo_2C/RGO (η_{onset} = 66 mV, b = 64 mV dec^{-1}) and W_2C/RGO (η_{onset} = 76 mV, b = 93 mV dec^{-1}) (Fig. 5b and Table S5†). Besides, the Tafel slope of Mo_2C–W_2C/RGO-0.56 within the theoretical value indicates that the reaction kinetics for hydrogen generation is the Volmer–Heyrovsky mechanism.[54,55] Furthermore, capacitance values (Fig. S9 and Table S5†), Nyquist diagram (Fig. 5d), and j_0 (Table S5†) confirm that the Mo_2C–W_2C/RGO-0.56 electrode has the largest

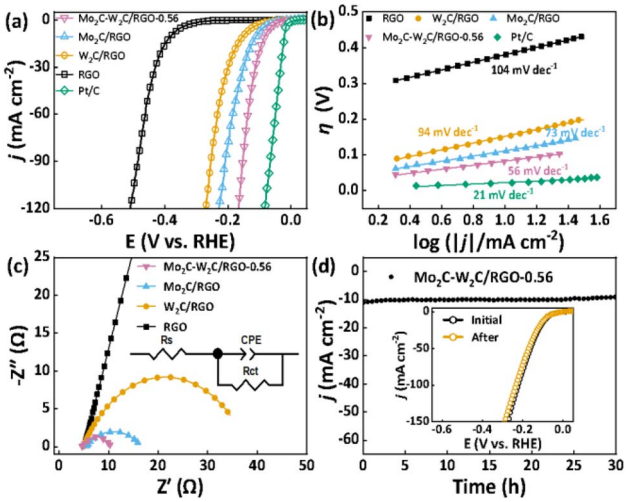

Fig. 4 Electrochemical measurements of Mo_2C–W_2C/RGO-0.56 for the HER in 0.5 M H_2SO_4. (a) Polarization curve and (b) Tafel plot of Mo_2C–W_2C/RGO-0.56 in comparison with those of 20 wt% Pt/C, Mo_2C/RGO, W_2C/RGO and RGO alone. (c) Electrochemical impedance spectrum of Mo_2C–W_2C/RGO-0.56 at η = 200 mV in comparison with those of Mo_2C/RGO, W_2C/RGO and RGO. The inset of panel c shows the equivalent circuit diagram. (d) Long-term durability test of Mo_2C–W_2C/RGO-0.56. The inset shows the LSV curves before and after the durability test.

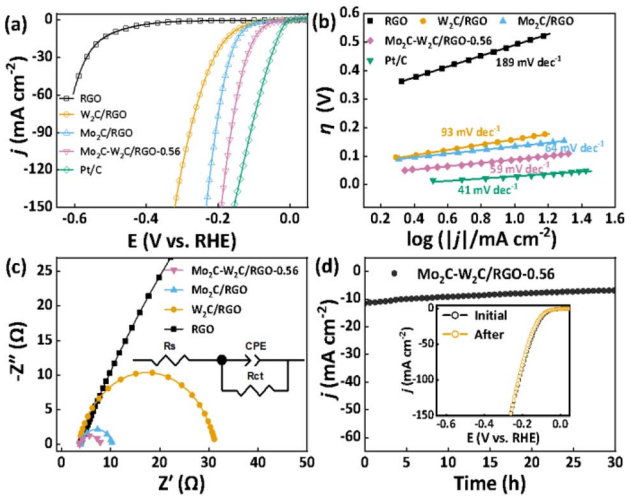

Fig. 5 Electrochemical measurements of Mo_2C–W_2C/RGO-0.56 for the HER in 1.0 M KOH. (a) Polarization curve and (b) Tafel plot of Mo_2C–W_2C/RGO-0.56 in comparison with those of 20 wt% Pt/C, Mo_2C/RGO, W_2C/RGO and RGO alone. (c) Electrochemical impedance spectrum of Mo_2C–W_2C/RGO-0.56 at η = 200 mV in comparison with those of Mo_2C/RGO, W_2C/RGO and RGO. The inset of panel c shows the equivalent circuit diagram. (d) Long-term durability test of Mo_2C–W_2C/RGO-0.56. The inset shows the LSV curves before and after the durability test.

electrochemical surface area, the smallest charge transfer impedance, and higher intrinsic activity, which is consistent with its HER activity. At the same time, Mo_2C–W_2C/RGO-0.56 also has satisfactory long-term stability in 1.0 M KOH, delivering a current density of about -10 mA cm^{-2} for 30 h. In addition, SEM analysis results (Fig. S10†) prove that the structure of Mo_2C–W_2C/RGO is well maintained after a long-term HER process, which further confirms the remarkable stability of Mo_2C–W_2C/RGO. Remarkably, the Mo_2C–W_2C/RGO delivers prominent HER activity in 1.0 M KOH, representing one of the current best carbide-based HER catalysts (Table S3†). All of these results indicate that Mo_2C–W_2C/RGO shows excellent hydrogen production performance over the entire pH range, providing a promising HER electrocatalyst for practical application.

The aforementioned results indicate the formation of the Mo_2C–W_2C heterostructure coupled with RGO, which shows superior acidic and alkaline HER performance. The origin of the efficient HER activity of Mo_2C–W_2C/RGO is worthy of investigation. Therefore, a series of control samples, including W_2C, Mo_2C, and Mo_2C–W_2C (Fig. S11a, c and e†), were constructed in the absence of GO, in addition to the RGO, W_2C/RGO and Mo_2C/RGO already mentioned. Electrochemical tests were performed to compare the activity of the HER under acidic and alkaline conditions. The poor performance of the RGO indicates that RGO is not an active component (Fig. S12†). In addition, W_2C/RGO and Mo_2C/RGO show superior HER activity over W_2C and Mo_2C, respectively, and the HER activity of Mo_2C–W_2C/RGO is better than that of Mo_2C–W_2C. The results indicate the positive role of RGO in the improvement of the HER performance. This is related to the good electrical conductivity and large surface area of RGO. In the case of the catalysts without a graphene substrate, W_2C, Mo_2C, and Mo_2C–W_2C catalysts exhibit severe agglomeration and accumulation (Fig. S11b, d and f†). The good coupling between graphene and nanoparticles inhibits the agglomeration of nanosheets and plays a good dispersion role, which helps to improve the active surface area of the catalyst and expose the active site. Furthermore, graphene as a good conductor can effectively reduce the interfacial barrier of electron transfer, which is helpful for the enhancement of reaction kinetics. The improved activity of Mo_2C–W_2C/RGO over Mo_2C/RGO and W_2C/RGO implies the important role of the heterostructure for the HER due to its strong electronic interaction. Thus, we propose that the Mo_2C–W_2C heterostructure is the main active component, and RGO is also an important factor because of its role in exposing the active site, as well as in mass/charge transfer.

To gain a fundamental understanding of the high catalytic activity of the Mo_2C–W_2C heterostructure for the HER, density functional theory (DFT) calculations were performed. Here, the free energy profiles of H adsorption on the (001) surface of pure W_2C (Fig. 6a) and Mo_2C (Fig. 6b), along with the corresponding surfaces of Mo_2C–W_2C (Fig. 6c) were computed. Regarding the overall HER rate, the hydrogen adsorption free energy (ΔG_{H^*}) is regarded as a good descriptor to evaluate the activity of the material, and optimal HER catalysts should have ΔG_{H^*} close to zero.[58–62] As illustrated in Fig. 6d, on the W site of W_2C, the ΔG_{H^*} is calculated to be -0.32 eV, and the ΔG_{H^*} on the Mo site of Mo_2C is -0.10 eV. The relatively negative ΔG_{H^*} on the W site shows that the strong adsorption of H on the surface of W_2C

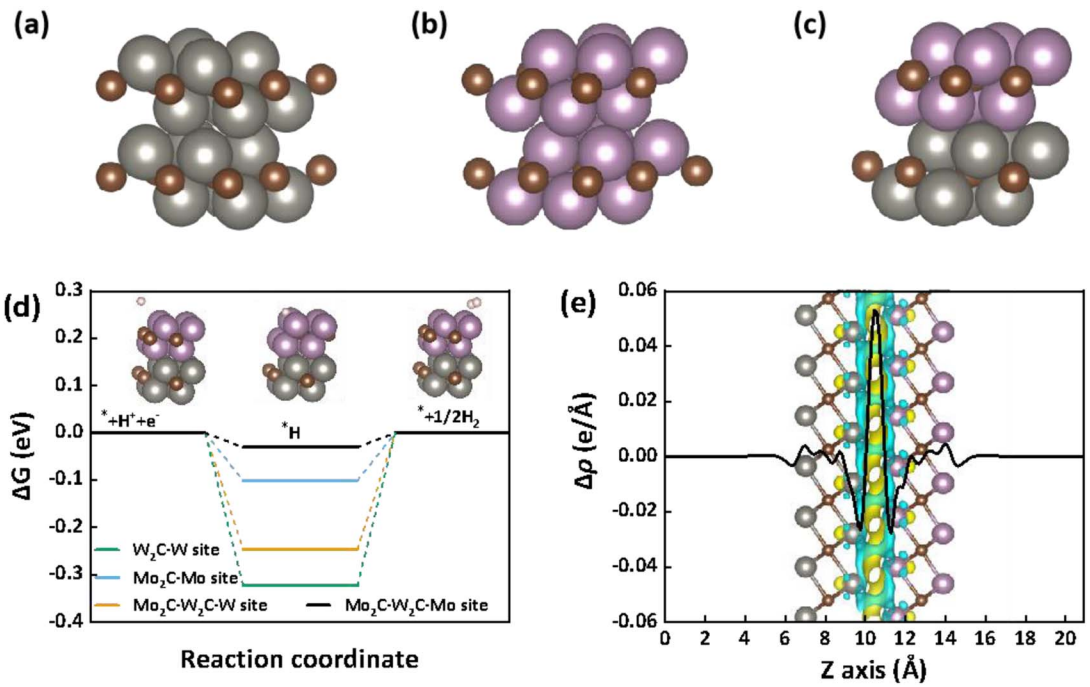

Fig. 6 Schematic model of (a) W_2C (001), (b) Mo_2C (001), and (c) Mo_2C–W_2C. (d) Calculated free energy diagram of H adsorption. (e) PA-CDD and CDD of the Mo_2C–W_2C. The yellow and cyan areas represent an increase and decrease in charge density, respectively. The purple, grey, brown, and pink spheres denote Mo, W, C, and H atoms, respectively.

restricts the Heyrovsky process, resulting in a low HER efficiency, which is consistent with our experimental results of electrochemical tests. For Mo_2C–W_2C, the ΔG_{H^*} values on the Mo and W sites of Mo_2C–W_2C are −0.03 eV and −0.25 eV, respectively, both of which are closer to the ideal ΔG_{H^*} (0 eV) than the corresponding Mo and W sites on pure Mo_2C and pure W_2C. The calculations demonstrate that the interface structure of Mo_2C–W_2C plays a crucial role in its excellent HER activity.

Additionally, we have calculated the charge-density differences (CDD) as well as the planar-average charge-density difference (PA-CDD) along the Z direction of the heterostructure to evaluate interfacial charge-transfer processes. As shown in Fig. 6e, the electron accumulation (yellow) and depletion (cyan) are concentrated at the interfaces formed between Mo_2C and W_2C, indicating the strong charge redistribution at the interface, consistent with the electron modulation observed by XPS (Fig. 3c and d). Fig. S13† displays the total density of states (DOS) of the Mo_2C, W_2C and Mo_2C–W_2C. The DOSs of all three materials cross their Fermi level (corresponding to the energy of the highest electron occupied orbital of the material), demonstrating that all of them can possess good conductivity during the HER. The high density of states of Mo_2C–W_2C adjacent to the negative side of the Fermi level further proves its excellent ability to donate electrons during the electrocatalytic HER process. The better HER activity of Mo_2C–W_2C may also originate from the interface charge distribution. This charge redistribution adjusts the surface electronic structure of the material, which weakens the H adsorption and facilitates H_2 desorption resulting in enhanced HER kinetics and reduced overpotential.

Based on all the above experiments and theoretical calculation results, the remarkable electrocatalytic activity and stability of Mo_2C–W_2C for the HER can be attributed to the following reasons: (i) the material is supported by graphene sheets with good electrical conductivity and large specific surface area, showing ultra-fine and evenly distributed nanoparticle morphology, high ECSA and good electron transport capacity, which is conducive to the transport of reactants and products, thus accelerating the occurrence of the HER. (ii) The optimized electronic structure at the Mo_2C–W_2C interfaces improves the kinetics of the hydrogen evolution process, which endows the Mo_2C–W_2C with enhanced kinetics and high activity.

Conclusions

In summary, an ultrafine and interface-rich Mo_2C–W_2C heterostructure anchored to reduced graphene oxide is successfully prepared and used as a highly efficient electrocatalyst for pH-universal HER. The ultrafine size and abundant interfaces of the Mo_2C–W_2C heterostructure maximize the exposure of active sites and facilitate the mass transfer process, while the interfacial interaction optimizes the electronic configuration of the catalyst. As a result, the Mo_2C–W_2C heterostructure afforded ultra-low overpotentials (η_{10} = 81 and 87 mV for reaching a current density of −10 mA cm^{-2}) under acidic and alkaline conditions. DFT calculations further indicate that the constructed Mo_2C–W_2C heterostructure can achieve almost ideal ΔG_{H^*} for the HER. In addition, the charge density difference analysis also reveals the modulating effect of the electronic structure of the heterostructures. The adjusted electronic structures of the Mo_2C–W_2C effectively promotes the desorption step of H*, which is responsible for the enhanced kinetic metrics and high HER activity of the Mo_2C–W_2C heterostructure. Both experiments and theoretical calculations have confirmed that the electrocatalytic HER performance of materials can be effectively modulated by adjusting the nanoarchitectures and electronic structure of carbides. This work provides good guidance for the future design of advanced materials with superior HER activity.

Author contributions

All authors have contributed to the preparation of the manuscript and given approval to the final version of the manuscript.

Conflicts of interest

There are no conflicts to declare.

Acknowledgements

This work was supported by the National Natural Science Foundation of China (Grant No. 22273066, 22173069), Shanghai Municipal Natural Science Foundation (Grant No. 19DZ2271500, 21ZR1467800) and the Fundamental Research Funds for the Central Universities.

References

1 X. Zou and Y. Zhang, *Chem. Soc. Rev.*, 2015, **44**, 5148–5180.
2 T. Kou, S. Wang and Y. Li, *ACS Mater. Lett.*, 2021, **3**, 224–234.
3 T. Ouyang, Y.-Q. Ye, C.-Y. Wu, K. Xiao and Z.-Q. Liu, *Angew. Chem., Int. Ed.*, 2019, **58**, 4923.
4 L. Jiang, R. Wang, Z. Xiang and X. Wang, *Int. J. Hydrogen Energy*, 2024, **11**, 898–906.
5 R. Mohili, N. R. Hemanth, H. Jin, K. Lee and N. Chaudhari, *J. Mater. Chem. A*, 2023, **11**, 10463–10472.
6 G. Zhao, K. Rui, S. X. Dou and W. Sun, *Adv. Funct. Mater.*, 2018, **28**, 1803291.
7 P. Quaino, F. Juarez, E. Santos and W. Schmickler, *Beilstein J. Nanotechnol.*, 2014, **5**, 846.
8 F. Li, G.-F. Han, H.-J. Noh, Y. Lu, J. Xu, Y. Bu, Z. Fu and J.-B. Baek, *Angew. Chem., Int. Ed.*, 2018, **57**, 14139–14143.
9 W. Li, Z.-Y. Hu, Z. Zhang, P. Wei, J. Zhang, Z. Pu, J. Zhu, D. He, S. Mu and G. V. Tendeloo, *J. Catal.*, 2019, **375**, 164–170.
10 Q. Xue, X. Y. Bai, Y. Zhao, Y. N. Li, T. J. Wang, H. Y. Sun, F. M. Li, P. Chen, P. Jin, S. B. Yin and Y. Chen, *J. Energy Chem.*, 2022, **65**, 94–102.
11 Z. Chen, X. Duan, W. Wei, S. Wang and B.-J. Ni, *J. Mater. Chem. A*, 2019, **7**, 14971–15005.
12 R. Wang, L. Jiang, Q. Wang, G. F. Wei and X. Wang, *Adv. Compos. Hybrid Mater.*, 2023, **6**, 157.

13 S. Hussain, D. Vikraman, A. Feroze, W. Song, K.-S. An, H.-S. Kim, S.-H. Chun and J. Jung, *Front. Chem.*, 2019, **7**, 716.
14 A. Nadar, A. M. Banerjee, M. R. Pai, R. P. Antony, A. K. Patra, P. U. Sastry, H. Donthula, R. Tewari and A. K. Tripathi, *Int. J. Hydrogen Energy*, 2020, **45**, 12691–12701.
15 R. B. Levy and M. Boudart, *Science*, 1973, **181**, 547–549.
16 X. F. Lu, L. Yu, J. Zhang and X. W. Lou, *Adv. Mater.*, 2019, **31**, 1900699.
17 Q. Gao, W. Zhang, Z. Shi, L. Yang and Y. Tang, *Adv. Mater.*, 2019, **31**, 1802880.
18 B. Ren, D. Li, Q. Jin, H. Cui and C. Wang, *J. Mater. Chem. A*, 2017, **5**, 13196–13203.
19 H. Jin, J. Chen, S. Mao and Y. Wang, *ACS Appl. Mater. Interfaces*, 2018, **10**, 22094–22101.
20 N. Han, K. R. Yang, Z. Lu, Y. Li, W. Xu, T. Gao, Z. Cai, Y. Zhang, V. S. Batista, W. Liu and X. Sun, *Nat. Commun.*, 2018, **9**, 924.
21 W.-F. Chen, J. T. Muckermana and E. Fujita, *Chem. Commun.*, 2013, **49**, 8896–8909.
22 X. Tao, Y. Li, J. Du, Y. Xia, Y. Yang, H. Huang, Y. Gan, W. Zhang and X. Li, *J. Mater. Chem.*, 2011, **21**, 9095–9102.
23 Y. Hu, B. Yu, W. Li, M. Ramadoss and Y. Chen, *Nanoscale*, 2019, **11**, 4876–4884.
24 W. Zheng, L. Wang, F. Deng, S. A. Giles, A. K. Prasad, S. G. Advani, Y. Yan and D. G. Vlachos, *Nat. Commun.*, 2017, **8**, 418.
25 W.-F. Chen, S. Iyer, S. Iyer, K. Sasaki, C.-H. Wang, Y. Zhu, J. T. Muckerman and E. Fujita, *Energy Environ. Sci.*, 2013, **6**, 1818.
26 P. Yan, Y. Wu, X. Wei, X. Zhu and W. Su, *Nanomaterials*, 2020, **10**, 1621–1711.
27 J. P. Perdew, K. Burke and M. Ernzerhof, *Phys. Rev. Lett.*, 1996, **77**, 3865.
28 G. Kresse and J. Furthmüller, *Comput. Mater. Sci.*, 1996, **6**, 15.
29 G. Kresse and J. Furthmüller, *Phys. Rev. B: Condens. Matter Mater. Phys.*, 1996, **54**, 11169.
30 G. Kresse and D. Joubert, *Phys. Rev. B: Condens. Matter Mater. Phys.*, 1999, **59**, 1758.
31 H. J. Monkhorst and J. D. Pack, *Phys. Rev. B: Condens. Matter Mater. Phys.*, 1976, **13**, 5188.
32 S. Grimme, J. Antony, S. Ehrlich and H. Krieg, *J. Chem. Phys.*, 2010, **132**, 154104.
33 S. Grimm, S. Ehrlich and L. Goerigk, *J. Comput. Chem.*, 2011, **32**, 1456–1465.
34 D. R. Lide, *CRC Handbook of Chemistry and Physics*, CRC Press, Boca Raton, FL, 2003.
35 F. Malara, S. Carallo, E. Rotunno, L. Lazzarini, E. Piperopoulos, C. Milone and A. Naldoni, *ACS Catal.*, 2017, **7**, 4786–4795.
36 Z. Zheng, S. Hu, W. Yin, J. Peng, R. Wang, J. Jin, B. He, Y. Gong, H. Wang and H. J. Fan, *Adv. Energy Mater.*, 2023, 2303064.
37 D. Guo, M. Yang, S. Xu, S. Zhu, G. Liu, N. Wu, A. Cao, H. Mi and X. Liu, *Nanoscale*, 2022, **14**, 14575–14584.
38 Y. Shen, Y. Jiang, Z. Yang, J. Dong, W. Yang, Q. An and L. Mai, *Adv. Sci.*, 2022, **9**, 2104504.
39 Y. Sun, X. Hu, J. C. Yu, Q. Li, W. Luo, L. Yuan, W. Zhang and Y. Huang, *Energy Environ. Sci.*, 2011, **4**, 2870–2877.
40 Q. Gong, Y. Wang, Q. Hu, J. Zhou, R. Feng, P. N. Duchesne, P. Zhang, F. Chen, N. Han, Y. Li, C. Jin, Y. Li and S.-T. Lee, *Nat. Commun.*, 2016, **7**, 13216.
41 Y. Zhao, K. Kamiya, K. Hashimoto and S. Nakanishi, *J. Am. Chem. Soc.*, 2015, **137**, 110.
42 J. G. Speight, *Lange's Handbook of Chemistry*, McGraw-Hill, Professional, New York, NY, USA, 16 edn, 2005.
43 H. Lin, W. Zhang, Z. Shi, M. Che, X. Yu, Y. Tang and Q. Gao, *ChemSusChem*, 2017, **10**, 2597–2604.
44 Y. Hu, B. Yu, W. Li, M. Ramadoss and Y. Chen, *Nanoscale*, 2019, **11**, 4876–4884.
45 W. Ding, Z. Wei, S. Chen, X. Qi, T. Yang, J. Hu, D. Wang, L.-J. Wan, S. F. Alvi and L. Li, *Angew. Chem., Int. Ed.*, 2013, **52**, 11755.
46 M. Shi, W. Li, J. Fang, Z. Jiang, J. Gao, Z. Chen, F. Sun and Y. Xu, *Electrochim. Acta*, 2018, **283**, 834–841.
47 Y. Ding, K. W. Cao, J. W. He, F. M. Li, H. Huang, P. Chen and Y. Chen, *Chin. J. Catal.*, 2022, **43**, 1535–1543.
48 Z. Kou, T. Wang, H. Wu, L. Zheng, S. Mu, Z. Pan, Z. Lyu, W. Zang, S. J. Pennycook and J. Wang, *Small*, 2019, **15**, 1900248.
49 P. Wei, X. Sun, M. Wang, J. Xu, Z. He, X. Li, F. Cheng, Y. Xu, Q. Li, J. Han, H. Yang and Y. Huang, *ACS Appl. Mater. Interfaces*, 2021, **13**, 53955–53964.
50 H. Yan, Y. Xie, Y. Jiao, A. Wu, C. Tian, X. Zhang, L. Wang and H. Fu, *Adv. Mater.*, 2018, **30**, 1704156.
51 S.-C. Sun, F.-X. Ma, H. Jiang, M.-X. Chen, P. Xu, L. Zhen, B. Song and C.-Y. Xu, *Chem. Eng. J.*, 2023, **462**, 142132.
52 J. Wang, F. Xu, H. Jin, Y. Chen and Y. Wang, *Adv. Mater.*, 2017, **29**, 1605838.
53 S. Xu, F. Wang, L. Mai, L. Wang and P. K. Chu, *Electrochim. Acta*, 2013, **90**, 344–349.
54 J. Yu, W.-J. Li, H. Zhang, F. Zhou, R. Li, C.-Y. Xu, L. Zhou, H. Zhong and J. Wang, *Nano Energy*, 2019, **57**, 222–229.
55 J. Zhao, N. Liao and J. Luo, *J. Mater. Chem. A*, 2023, **11**, 9682–9690.
56 Z. Li, M. Hu, P. Wang, J. Liu, J. Yao and C. Li, *Coord. Chem. Rev.*, 2021, **439**, 213953.
57 Z. Pu, I. S. Amiinu, R. Cheng, P. Wang, C. Zhang, S. Mu, W. Zhao, F. Su, G. Zhang and S. Liao, *Nano-Micro Lett.*, 2020, **12**, 1–29.
58 J. K. Nørskov, T. Bligaard and A. Logadottir, *J. Electrochem. Soc.*, 2005, **152**, 23–26.
59 J. Greeley, T. F. Jaramillo, J. Bonde, I. Chorkendorff and J. K. Nørskov, *Nat. Mater.*, 2006, **5**, 909–913.
60 H. J. Yan, Y. Xie, A. P. Wu, Z. C. Cai, L. Wang, C. G. Tian, X. M. Zhang and H. G. Fu, *Adv. Mater.*, 2019, **31**, 1901174.
61 L. Wang, Y. Hao, L. Deng, F. Hu, S. Zhao, L. Li and S. Peng, *Nat. Commun.*, 2022, **13**, 5785.
62 E. Yu and Y. Pan, *J. Mater. Chem. A*, 2022, **10**, 24866–24876.

